RESOURCE GEOLOGY · WILEY

ASTER mapping of gypsum deposits of Thumrait region of southern Oman

Sankaran Rajendran[1] 🟢 | Sobhi Nasir[2]

[1]Environmental Science Center, Qatar University, Doha, Qatar

[2]Earth Science Research Center, Sultan Qaboos University, Muscat, Oman

Correspondence
Sankaran Rajendran, Environmental Science Center, Qatar University, P.O. Box: 2713, Doha, Qatar.
Email: srajendran@qu.edu.qa

Abstract

This study demonstrates the use of ASTER data for the mapping of gypsum deposits and associated geological formations that occurred in the Thumrait region of southern Oman. The measurement of spectra over samples of gypsum in the 1,300–2,500 nm wavelength using a PIMA spectrometer showed the presence of distinct absorptions at 1400–1600, 1750, 1940, 2,100, and 2,400 nm characteristics to O—H stretching, H_2O combinations, and S—O bending overtones and stretching, respectively. Studying the unique spectral absorption characters of gypsum samples, we developed a false color composite (FCC) and an image by decorrelation stretch using the spectral bands 7, 3, and 2 of ASTER. The results FCC showed the regions of gypsum occurrences, and the decorrelated image discriminated the gypsum occurrences from other geological formations of the area. The study of surface mineralogy of the region using the VNIR-SWIR bands by the spectral angle mapper method showed the presence of sulfate, carbonate, and clay minerals of the geological formations in the study area. We compared the results of ASTER with the results obtained using spectral bands 12, 8, and 4 of Sentinel-2A processed by the same methods. The study showed that the spectral bands of ASTER can be used for mapping the gypsum and associated geological formations.

KEYWORDS
Sentinel-2A, gypsum, mapping, spectral absorption, image processing, Sultanate of Oman

1 | INTRODUCTION

Literature review shows that the spectral resolutions in six SWIR bands of the advanced spaceborne thermal emission and reflection radiometer (ASTER) have been utilized for mapping of surface mineralogy, hydrothermal alteration zones, and geological formations of the arid region where no vegetation and surface mineralogy is directly exposed to the sensor (Hunt and Salisbury, 1971; Hunt, 1977; Yamaguchi *et al.*, 1998; Abrams, 2000; Mars and Rowan, 2010; Tangestani *et al.*, 2011; Pour and Hashim, 2012; Hosseinjani Zadeh *et al.*, 2014; Rajendran and Nasir, 2019). Lithologies, structures, and minerals of the arid region have also been mapped using the Landsat TM, EMT +, and SPOT data (Abrams *et al.*, 1988; Gastellu-Etchegorry *et al.*, 1990; Matthews and Jones, 1992).

Several research studies showed the capability of Sentinel-2A data for estimating biophysical and biochemical parameters such as leaf area index (Richter *et al.*, 2009, 2012; Atzberger and Richter, 2012), chlorophyll and nitrogen biophysical parameters (Verrelst *et al.*, 2012; Frampton *et al.*, 2013), the red edge position (Clevers and Gitelson, 2013; D'Odorico *et al.*, 2013; Delegido *et al.*, 2013), and mapping of coral reefs (Hedley *et al.*, 2012) and water quality (Salama *et al.*, 2014). However, studies using Sentinel-2A data for geological applications of the arid region are fewer. van der Meer *et al.* (2014) discussed the geological applications of Sentinel-2 and van der Werff and van der Meer (2015) evaluated the applicability of the data for iron detection. The authors stated that the Sentinel-2 MSI (multispectral instrument) has higher spatial resolution compared to Landsat and that it provides several relatively narrow bands in the VNIR region. Al-Nahmi *et al.* (2017) studied the geology of Al Maghrabah area—Hajjah region, Yemen using Sentinel-2 data. The authors processed the data by optimum index factor (OIF), independent component analysis (ICA), and minimum noise fraction (MNF) methods and showed the geology of the region as four units, namely, the basement rocks (meta-volcanic, meta-sediments), sedimentary rocks, intrusive rocks, and volcanic rocks. They stated that the data and method used have great potential for lithological mapping. Recently, Ge *et al.* (2018a) discriminated the lithology of Shibanjing ophiolite complex of Beishan Orogenic in Inner Mongolia, China using ASTER and Sentinel-2A data. The authors used the band ratio, principal components analysis (PCA), MNF, and support vector machine (SVM) methods and stated that the Sentinel-2A data outperformed ASTER in the lithological mapping of the Shibanjing ophiolite complex.

The Sentinel-2A provides two bands with broad bandwidth in SWIR region, which can be utilized in geological research (Mielke *et al.*, 2014; van der Meer *et al.*, 2014; van der Werff and van der Meer, 2015; Al-Nahmi *et al.*, 2017; Costa *et al.*, 2017; Cardoso-Fernandes *et al.*, 2018; Ge *et al.*, 2018b). Especially, the spectral band 12 which has 2,112.9–2,286.5 nm wavelength characteristic to S—O bending overtones (Cloutis *et al.*, 2006) or OH/H$_2$O combinations and/ or overtones (Hunt *et al.*, 1971; Cloutis *et al.*, 2008) and 20 m spatial resolution (Padró *et al.*, 2018) can be used with other bands to map gypsum (calcium sulfate dehydrate—CaSO$_4$ 2H$_2$O) occurrences. This study characterizes the spectral absorption features of gypsum mineral and discriminates the layered gypsum deposits and associated geological formations occurring in the Thumrait region of the Sultanate of Oman using the ASTER data. The study compares the results of ASTER data with the results obtained using the Sentinel-2A data.

2 | GEOLOGY OF STUDY AREA

The study area is situated near Thumrait of southern Oman (Figure 1). Geologically, the area is covered by sedimentary formations of Tertiary and Quaternary ages. The sequences of formations are given in Figure 2. It shows the occurrence of thin-bedded dolomites with nodular chert, silica geodes, and small echinoderms of the Mudayy Member of Umm Formation (Eum) (Paleocene to Early Eocene) at the base of the area. This formation is overlain by a formation of Aybut Member (Er1) that consists of recrystallized breccia and chalky dolomite, bedded chert, and flint belong to the lower unit of and a formation of the lower part of Gahit Members (Er2) that occurs with partly recrystallized white chalky dolomite, collapsed breccia, chert with marl, and bioclastic limestone. The formations are underlain by Suddah evaporate deposits (Erg) of Rus Formation. The deposits contain laminated gypsums with intercalations of dolomite, biocalcarenite, and bedded chert and flint. Sequentially, the deposits are overlain by yellowish shale consist of intercalations of white to yellowish bioclastic limestone; green marl and coquina belong to Andhur Member (Eda) of Hadhramut Group. These Tertiary formations are overlain by Quaternary age deposits such as terrace alluvium (Qty) and wadi floor sands and gravels (Qty-z) (Figure 1; Ministry of Petroleum and Minerals, 1988). The study area has deposits of huge amounts of gypsum and mining of the gypsum is ongoing by several industries.

3 | SPECTRAL PROPERTIES OF CA-SULFATES

The reflectance spectra of Ca-sulfates, namely, gypsum (CaSO$_4$ 2H$_2$O), anhydrite (CaSO$_4$), and bassanite (2CaSO$_4$ H$_2$O) was first studied by Hunt *et al.* (1971) and later by Crowley (1991), Cloutis *et al.* (2006, 2008), and Clark *et al.* (2007). The authors identified spectral absorptions of such minerals near 1,000, 1,200, 1,400–1,600, 1750, 1940, 1970, 2,100–2,200, and 2,400 nm. Literature review shows that the absorption band near 1,000 nm in gypsum is due to a combination of the first overtone of the O—H stretching and the first overtone of the H—O—H bending fundamentals (Crowley, 1991). The absorption near 1,200 nm band to be a combination of the H$_2$O bending fundamental and the first overtone of the O—H stretching fundamental (Crowley, 1991). Cloutis *et al.* (2008) stated that the triplet absorption found between 1,400 and 1,600 nm arises from O—H stretching. Crowley (1991) and Cloutis *et al.* (2006, 2008) described that the absorption near 1750 nm was attributed to bending and stretching combinations of
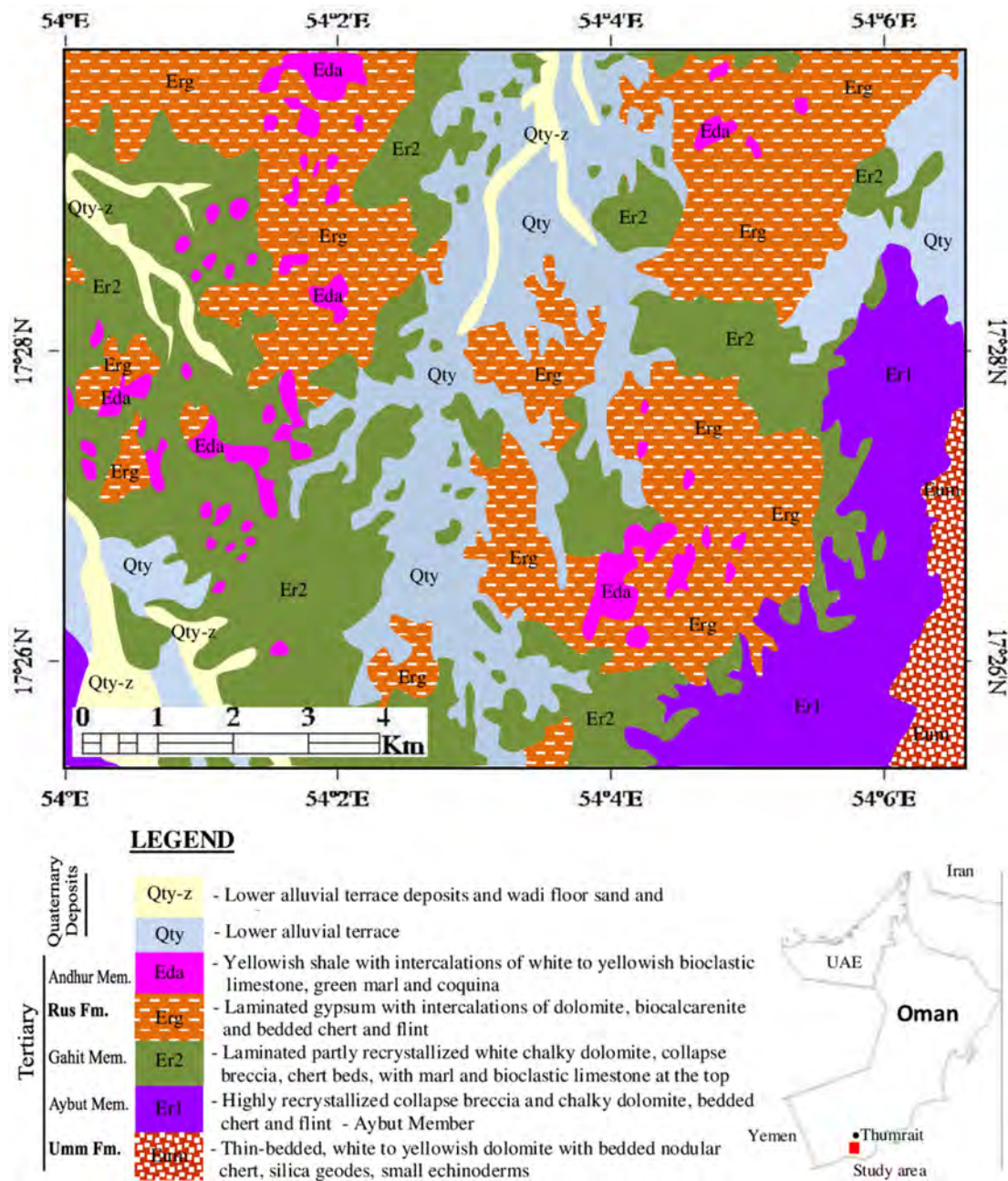
FIGURE 1 Geology of study area (Ministry of Petroleum and Minerals, 1988)

the H_2O molecule, while Hunt et al. (1971) states that this absorption may also be due to O—H bending and stretching or rotational fundamentals, or S—O bending overtones. The absorption bands near 1940 and 1970 nm in gypsum result from H_2O combinations (Crowley, 1991; Cloutis et al., 2008). Hunt et al. (1971) and Cloutis et al. (2006, 2008) described the absorptions of 2,100–2,200 nm range and stated that these are due to S—O bending overtones (Cloutis et al., 2006) or OH/H_2O combinations and/ or overtones. Cloutis et al. (2008) also stated that the absorption in the 2,400 nm arises from S—O stretching combinations.

Crowley (1991) compared the spectra of bassanite and gypsum and stated that many bands sufficiently differentiate the Ca-sulfate minerals. Cloutis et al. (2008) stated that the bassanite has only one H_2O/O—H absorption feature in the 1700–1800 nm regions while the gypsum has two. The authors also described the absorption of unknown origin near 2090 nm present in the bassanite, but not in gypsum. They also stated that the S—O and/or H_2O/O—H absorptions in the 2,200 nm region in gypsum are not seen in bassanite. Blaney and McCord (1995) and Bishop and Murad (2005) stated that the absorption features found near 4.3–5.3 μm are due to the presence of
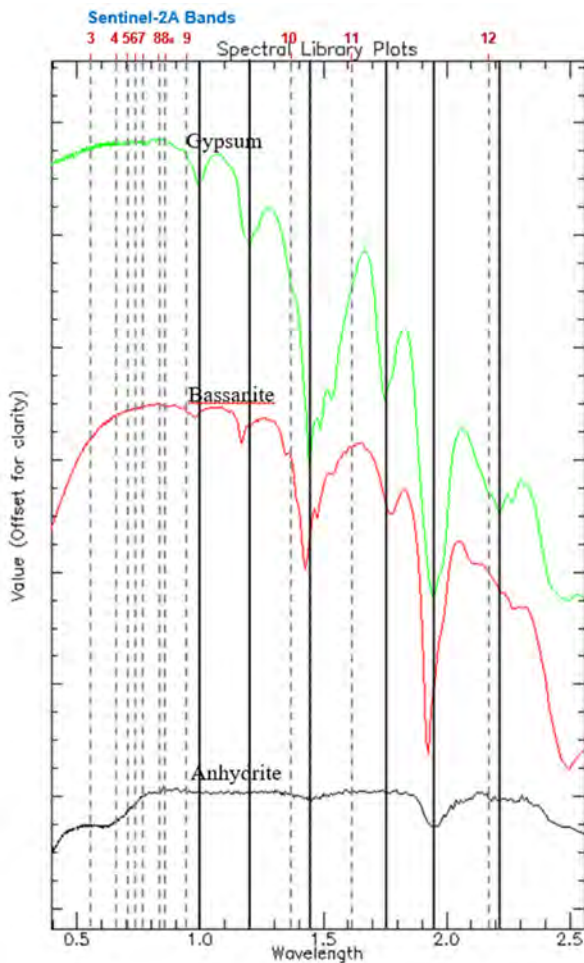
FIGURE 2 Spectral plot of sulfate minerals stacked form USGS spectral library for minerals. Dashed vertical lines represent spectral bands of sentinel-2A and the solid lines represent the wavelength absorptions of gypsum

Ca-sulfate. Figure 2 shows the spectra of the gypsum, bassanite, and anhydrite minerals taken from the United States Geological Survey (USGS) Spectral Library for minerals (using ENVI™) in the 0.3–2.5 μm region. The plot shows the spectral absorptions of gypsum (green spectra) near 1.0, 1.2, 1.4–1.6, 1.75, 1.9–2.0, and 2.1–2.2 μm wavelengths (solid vertical lines). The spectral absorptions of anhydrite (red) and bassanite (black) can be compared with the absorptions of the gypsum and studied with the position of Sentinel-2A bands (dashed vertical lines, Figure 2).

3.1 | Spectral absorptions of gypsum

In this study, more than 120 reflectance spectra are measured over the gypsum samples collected from sedimentary formations and mining industry region using a

Portable Infrared Mineral Analyzer (PIMA) spectrometer in the 1,300–2,500 nm wavelengths (see Section 4). The selected spectra of the samples are presented in Figures 3 and 4. The study of the spectra of industry gypsum (Figure 3a) shows the presence of triplet spectral absorptions in between 1,400–1,600 nm (Figure 3b), and distinct strong absorptions near 1750 nm (Figure 3c) and 1940 nm (Figure 3d) (vertical solid pink lines). The spectra exhibit shallow absorptions near 2,200 nm and 2,400 nm. The triplet absorptions found at 1450, 1495, and 1,530 nm (Figure 3b) between 1,400–1,600 nm arise from O—H stretching (Cloutis et al., 2008). The absorption near 1750 nm (Figure 3c) is due to bending and stretching combinations of the H_2O molecule or O—H bending and stretching or S—O bending overtones (Hunt et al., 1971; Crowley, 1991; Cloutis et al., 2006, 2008). The deep absorption occurred near the 1940 nm result from H_2O combinations (Clark et al., 1990; Crowley, 1991; Cloutis et al., 2008). The very shallow absorption found near 2,200 nm and the absorption centered near 2,400 nm (Figure 3b,e) are due to S—O bending overtones and stretching combinations, respectively (Clark et al., 1990; Cloutis et al., 2008). The spectra collected over the gypsum samples belonging to the sedimentary formations (Figure 4a) showed absorptions similar to the industry gypsums (Figure 4b-e). The study of the spectra of gypsum samples shows absorptions mainly due to O—H stretching, H_2O combinations and S—O bending overtones and stretching, and spectral bands of any sensor of satellite characteristics to such absorptions wavelengths have the potential to map gypsum occurrences. However, the absorptions around 1,500 nm and 1,900 nm are water vapor atmospheric absorption bands and cannot be well utilized, but the other absorption features at 1,750, 2,200, and 2,400 nm are well defined. Figure 5 presents a spectral plot of the industrial gypsum and the gypsum of sedimentary formations of the study area resampled to SWIR spectral bands (4 to 9) of ASTER in 1.3 to 2.5 μm (Rajendran et al., 2018; Rajendran et al., 2020). It shows clearly that the gypsums of study region have absorptions in the 2.2 and 2.4 μm (green and red elliptical) and the ASTER bands closer to the wavelengths can be used to discriminate gypsum occurrences.

Also, we measured the spectra of the samples of chalky dolomite, bioclastic limestone, and yellowish shale of the study area. The spectra of representative samples are given in Figure 6. The study of the spectra of chalky dolomite showed spectral absorptions near 1,400, 1900, 2,160, 2,335, and 2,490 nm (Figure 6a). The broad absorptions found near 1,400 and 1,900 nm are related to the presence of hydroxyl and water molecules contents, whereas the absorption near 2,160 nm and deep absorptions near 2,335 and 2,490 nm are due to the presence of
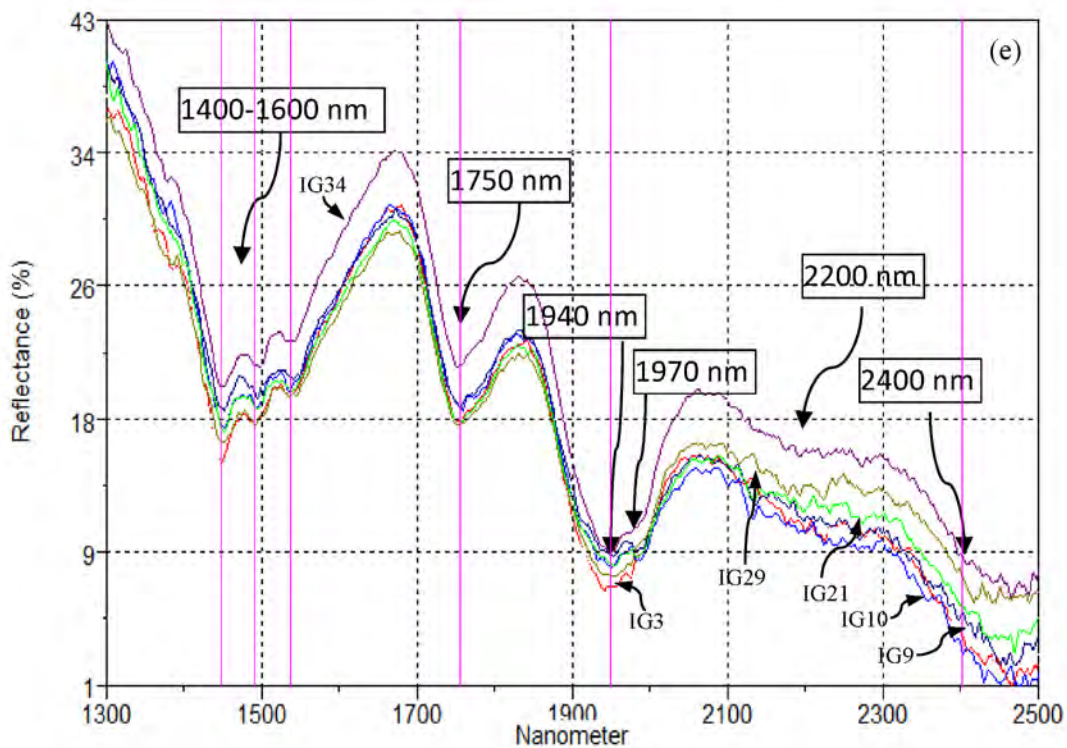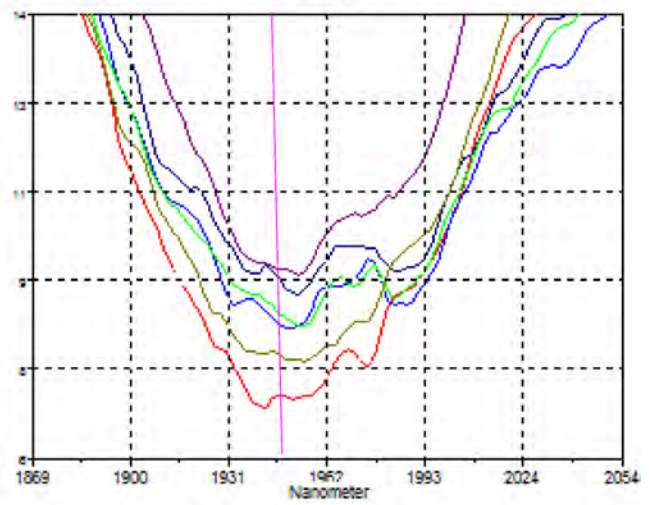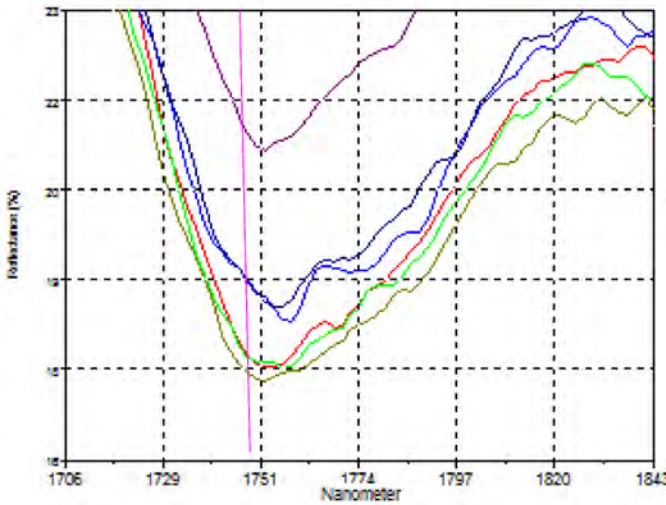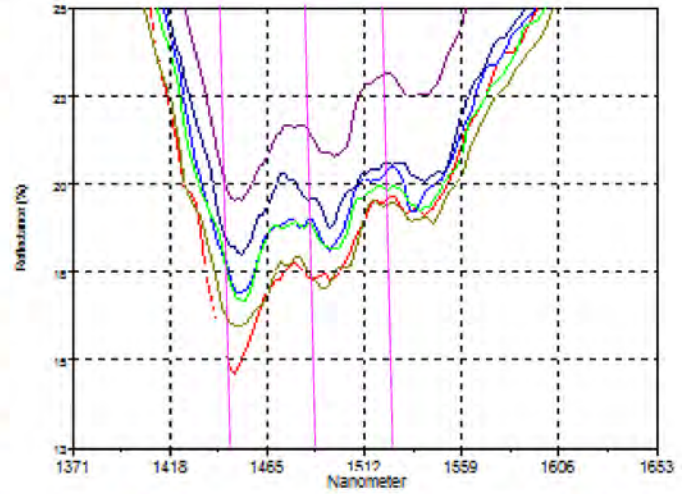
FIGURE 3 PIMA plots show spectral absorptions (pink lines) of industrial gypsum
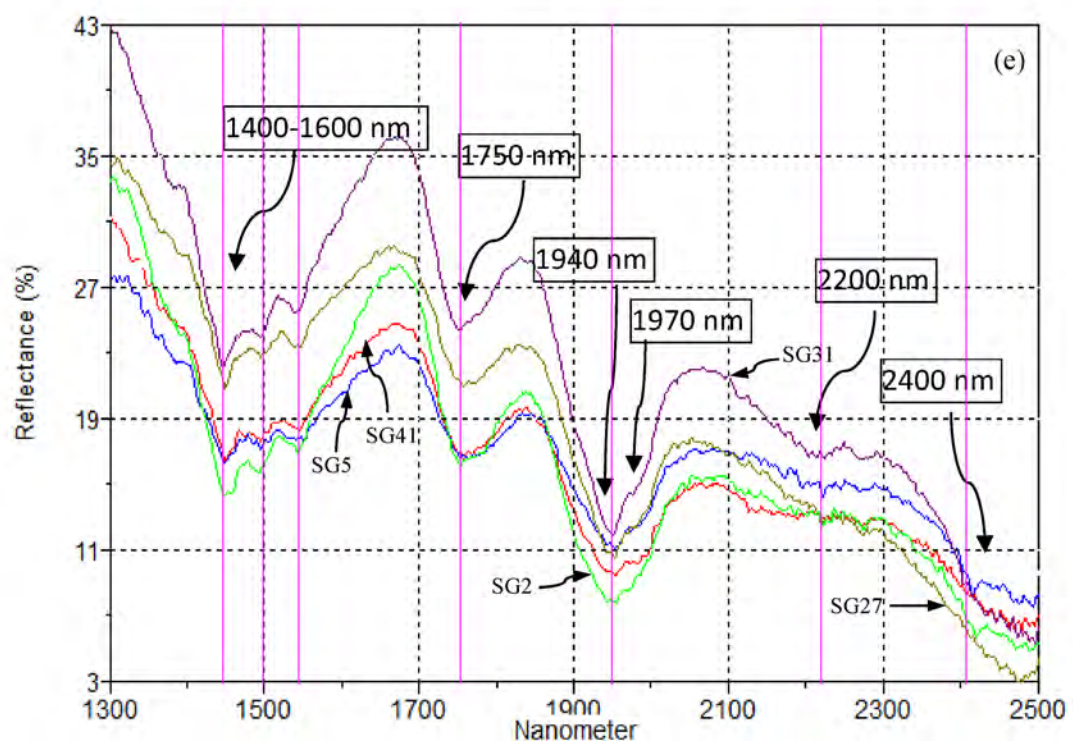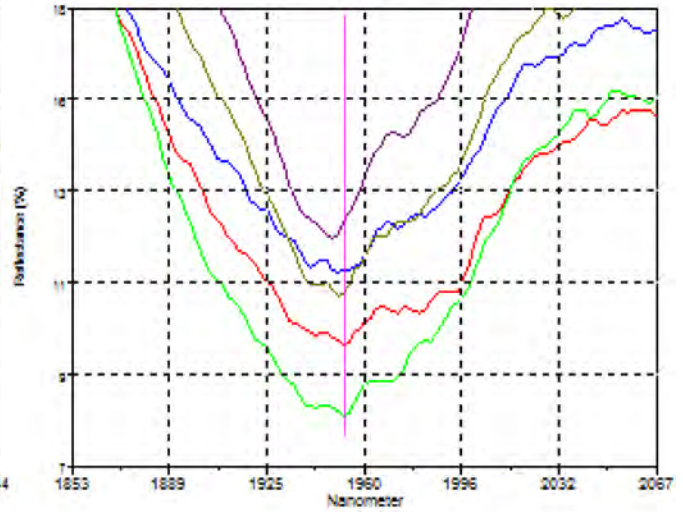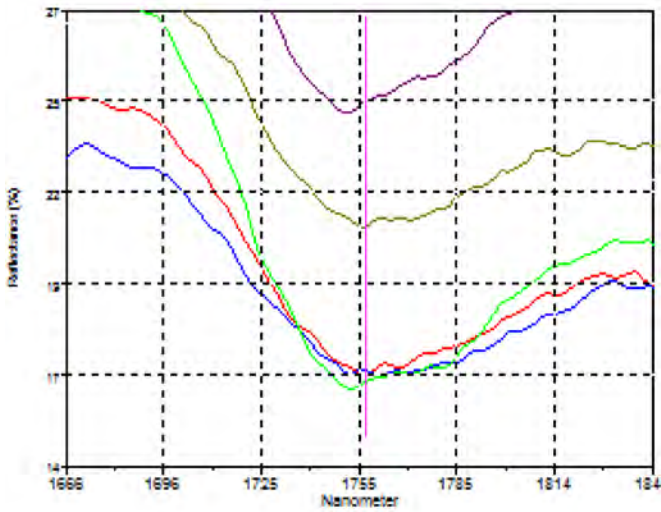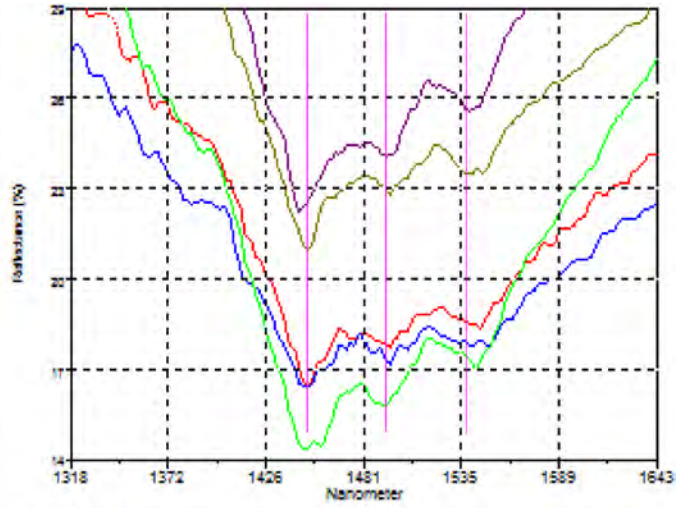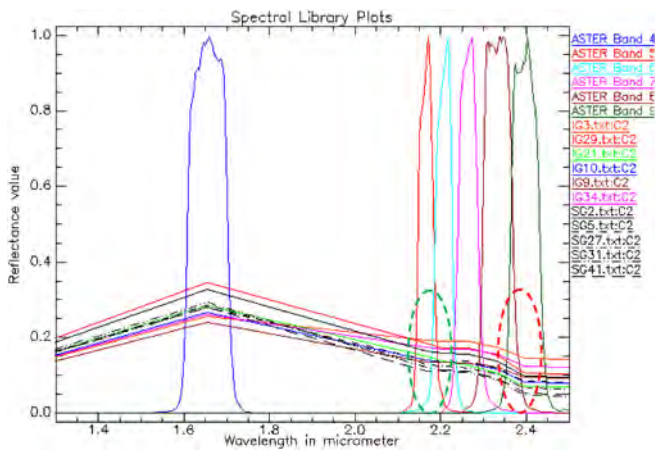
FIGURE 4   PIMA plots show spectral absorptions (pink lines) of gypsum of sedimentary occurrences

FIGURE 5 Spectra of the industrial gypsum (IG3 to IG34) and the gypsum of sedimentary formations (SG2 to SG41) resampled to SWIR spectral bands of ASTER in 1.3 to 2.5 μm

carbonate contents in the samples. The bioclastic limestone consists of calcites produced spectra similar to chalky dolomite except showing deep absorptions and differences in values near 2,345 and 2,495 nm (Figure 6b). The study of yellowish shale, which consists of illite and kaolinite showed spectral absorptions near 1,400, 1900, and 2,350 nm. The absorptions are due to the presence of hydroxyl, water, and Al-OH molecules in the samples (Figure 6c).

4 | SATELLITE DATA AND IMAGE PROCESSING METHODS

4.1 | Satellite data

In this study, we used data of ASTER and Sentinel-2A. ASTER is onboard Terra satellite and consists of three separate instrument subsystems: 1) visible and near-infrared (VNIR), 2) short-wavelength infrared (SWIR), and 3) thermal infrared (TIR). The VNIR subsystem has three recording channels between 0.52 and 0.86 μm with an additional backward-looking band for stereo construction of Digital Elevation Models (DEMs). It has a spatial resolution of 15 m. The SWIR subsystem has six recording channels between 1.6 and 2.43 μm at a spatial resolution of 30 m and the TIR subsystem has five recording channels covering the 8.12–11.65 μm at a spatial resolution of 90 m. The sensor characteristics of ASTER are provided in Table 1a (for further details see http://asterweb.jpl.nasa.gov/content/03_data/04_Documents/aster_user_guide_v2.pdf). In this study, the ASTER Level 1B image data acquired on November 30, 2001, is used. The data have a cloud cover of 0%. The data were supplied in terms of scaled radiance at the sensor with radiometric and geometric corrections
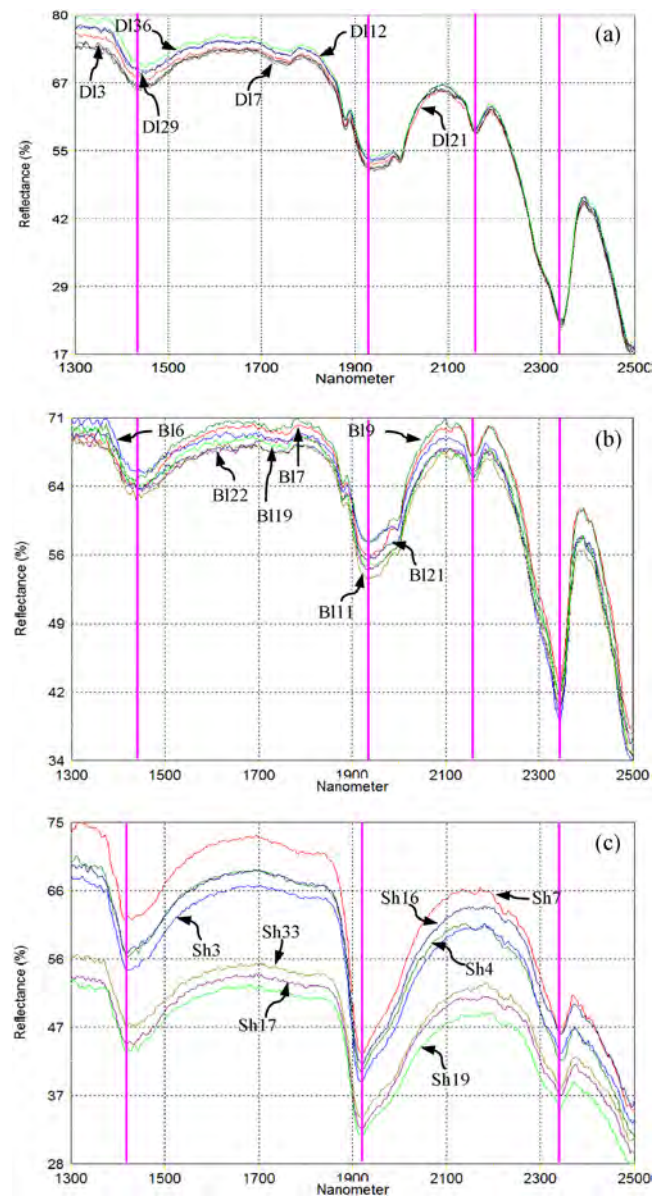
FIGURE 6 PIMA plots show spectral absorptions of (a) chalky dolomite. (b) bioclastic limestone. (c) yellowish shale of the Thumrait region

already applied. These are georeferenced to the WGS-84 ellipsoid (EPSG: 32640) and Universal Transverse Mercator (UTM) Zone 40 N projection similar to the Sentinel-2A data. A subset of nine VNIR and SWIR bands of ASTER cover the area were processed using ENVI™. During the pre-processing of the data, the atmospheric correction was applied to eliminate the spectral effect of water vapor and aerosols. The raw radiance data from the imaging spectrometer were rescaled to reflectance data using Fast Line-of-sight Atmospheric Analysis of Spectral Hypercubes (FLAASH) algorithm after the cross-track illumination correction. Both the Sentinel-2A and ASTER data were obtained from NASA Land Processes Distributed Active Archive Center User Services (https://LPDAAC.usgs.gov).

TABLE 1 (a) Sensor characters of ASTER (https://asterweb.Jpl.Nasa.Gov/characteristics.Asp) and (b) spectral position, bandwidth, and spatial resolution of Sentinel-2 bands according to the Copernicus derived user requirements (from van der Meer *et al.*, 2014)

(a) Sensors	Wavelength regions		
Characteristics	VNIR	SWIR	TIR
Spectral bands with range (μm)	Band 01 0.52–0.60	Band 04 1.6–1.7	Band 10 8.125–8.475
	Nadir looking		
	Band 02 0.63–0.69	Band 05 2.145–2.185	Band 11 8.475–8.825
	Nadir looking		
	Band 03N 0.76–0.86	Band 06 2.185–2.225	Band 12 8.925–9.275
	Nadir looking		
	Band 03B 0.76–0.86	Band 07 2.235–2.285	Band 13 10.25–10.95
	Backward looking		
		Band 08 2.295–2.365	Band 14 10.95–11.65
		Band 09 2.36–2.43	
Spatial resolution (m)	15	30	90
Swath width (km)	60	60	60
Radiometric Resol. (bits)	8	8	12
Cross track pointing	± 318 km (± 24 deg)	± 116 km (± 8.55 deg)	± 116 km (± 8.55 deg)

(b) Bands	Wavelength regions	Center wavelength (nm)	Band width (nm)	Spatial resolution (m)	Purpose
1		443	20	60	Atm. Correction (aerosol scattering)
2		490	65	10	Vegetation senescing, carotenoid, browning and soil background; atm. Correction (aerosol scattering)
3		560	35	10	Green peak, sensitive to total chlorophyll in vegetation
4		665	30	10	Max. Chlorophyll absorption
5		705	15	20	Red edge position; consolidation of atmospheric corrections/fluorescence baseline.
6	VNIR	740	15	20	Red edge position; atmospheric correction; retrieval of aerosol load
7		783	20	20	LAI; edge of the NIR plateau
8		842	115	10	LAI
8a		865	20	20	NIR plateau, sensitive to total chlorophyll, biomass, LAI and protein; water vapor absorption reference; retrieval of aerosol load and type
9		945	20	60	Atm. Correction (water vapor absorption)
10		1375	30	60	Atm. Correction (detection of thin cirrus)
11		1610	90	20	Sensitive to lignin, starch and forest above ground biomass; snow/ice/cloud separation
12	SWIR	2190	180	20	Assessment of Mediterranean vegetation conditions; distinction of clay soils for monitoring of soil erosion; distinction between live biomass, dead biomass and soil, e.g. for burn scars mapping

Abbreviation: LAI, leaf area index.

The Sentinel-2A is in a sun-synchronous orbit at 786 km altitude (14+ 3/10 revolutions per day) with a 10:30 a.m. descending node. This local time was selected as the best compromise between minimizing cloud cover and ensuring suitable sun illumination. It is close to the Landsat local overpass time and matches SPOT's, allowing the combination of data with historical images to build long-term time series. Sentinel-2A is a multispectral instrument that has large FOV (290 km), high revisit (5 days at the equator under the same viewing conditions), high spatial resolution (10 m, 20 m and 60 m), and 12-bit radiometric resolution. It has 13 spectral bands in the visible, near-infrared, and short wave infrared part of the electromagnetic spectrum. The four bands at 10 m resolution ensure compatibility with SPOT 4 and 5 and meet the user requirements for land cover classification. The 20 m resolution for six bands has been a requirement for other Level 2 processing such as scene classification and atmospheric correction. Bands at 60 m are mainly dedicated to atmospheric corrections and cloud screening (443 nm for aerosols retrieval, 940 nm for water vapor correction, and 1,375 nm for cirrus detection). The 60 m resolution is considered adequate to capture the spatial variability of the atmospheric geophysical parameters (Table 1a). All these bands support the continuity of the SPOT and Landsat missions and provide operational products such as land-cover maps, land-cover change detection maps, and geochemical/physical variables (Drusch *et al.*, 2012). The Copernicus Open Access Hub (previously known as Sentinels Scientific Data Hub) provides completely free access to Sentinel-2 data. This study uses the data of Sentinel-2A acquired on 26th September 2018. The data were pre-processed and georeferenced to the WGS-84 ellipsoid (EPSG: 32640) and Universal Transverse Mercator (UTM) Zone 40 N projection and layer staked using QGIS (3.4.0-Madeira). Further, the area of study is image processed for mapping of gypsum occurrences using ENVI™ software (version 5.3, Harris Geospatial Solutions, Broomfield, CO, USA). The results of mapping were studied and compared with the results obtained from the analyses of spectral bands acquired by ASTER over the same area.

4.2 | Image processing methods

To discriminate gypsum occurrences of the study area, the spectral bands 7, 3, and 2 of ASTER were used and developed a false color composite (FCC; R: 7; G: 3; B: 2). To map the geological formations associated with the gypsum occurrences, a decorrelation stretching method is applied (Rothery, 1987; Abrams *et al.*, 1988; Gillespie *et al.*, 1996). The method is a first-order mapping technique that enhances subtle spectral differences. Here, the original data values of selected bands are contrast-stretched and maximized to fill all the available color space, but the hues in the original red, green, and blue (RGB) combination are retained. The results of the FCC and decorrelation stretching method are compared with the results obtained using Sentinel-2A spectral bands 12, 8, and 4 processed by the same methods. The Sentinel-2A senses energy that comes from the earth surface in the visible near-infrared (VNIR) wavelength region (0.44 to 0.95 μm) in the spectral bands 1 to 9 (including band 8a) and in the shortwave infrared (SWIR) wavelength region (1.57 to 2.28 μm) in the spectral bands 10 to 12. Among the bands, the band 1 is dedicated to aerosol correction and band 10 is for the detection of cirrus clouds. We studied the center wavelengths of bands which are closer to the absorption wavelengths of major minerals and rocks of the study area, mainly the Ca-sulfate, carbonate, and hydroxyl bearing minerals and rocks such as gypsum, chalky dolomite, limestone, and yellowish shale, and processed them to map the gypsum occurrences of the study area.

Besides, we attempted to map the surface minerals of the gypsum deposits and associated geological formations using VNIR-SWIR spectral bands of ASTER by the Spectral Angle Mapper (SAM) method to map the minerals of the arid region. SAM method is one of the widely accepted and popular image processing techniques for hyperspectral image processing, which can also be used in lower spectral resolution systems (Rowan and Mars, 2003; Gabr *et al.*, 2010). It determines the spectral similarity between the spectra of each pixel and reference spectral end-members by calculating the angle between the vectors in a space with dimensionality equal to the number of bands (Yuhas *et al.*, 1992; Kruse *et al.*, 1993). It starts with reducing abundant information and data dimensionality using minimum noise fraction (MNF) transformation and then apply pixel purity index (PPI) mapping for the determination of purest pixels of the image and subsequently the end members (pixels) are extracted utilizing the n-Dimensional Visualizer tool. The extracted end members are then compared with known spectra of the USGS Spectral Library for minerals (Clark et al., 1993) loaded in the software to identify and prepare SAM classification (Kruse *et al.*, 1993; Gabr *et al.*, 2010).

In this study, VNIR-SWIR spectral bands of ASTER are processed using SAM. The hyperspectral tools applied to 10 bands initially determined the inherent dimensionality of MNF image data (Boardman and Kruse, 1994). The images found an increase in noise from MNF bands 1 to 10. These bands are further processed to determine the most spectrally pure (extreme) pixels containing mineral information of the image by PPI. The pixels were

determined by providing the PPI iteration value of 10,000 (the maximum), the threshold value of 2.5, and the SAM angle of 0.1 rad. The pixels are fully classified when increasing the SAM angle of 0.12 rad. The PPI records the extreme pixels in each projection (those pixels that fall onto the ends of the unit vector) and notes the total number of times each pixel marked as extreme and extracted the end members. The obtained pure pixels were typically corresponding to the mixing end members computed by repeatedly projecting n-D scatter plots on a random unit vector.

4.3 | Field study

The results of FCCs, decorrelation stretch, and SAM are verified in the field during fieldwork conducted in December 2018. During which traverse-based field samples, including minerals and rocks were collected from the geological formations. The samples were used to prepare microscopic thin sections to study the minerals of the formations under the microscope. Samples of chalky dolomite, bioclastic limestone, yellowish shales and gypsum found in the sedimentary formations and mining regions were used to measure reflectance spectra using a portable infrared mineral analyzer (PIMA) spectrometer. The instrument is fabricated for field spectroscopy by Integrated Spectronics Pty Ltd., Australia. The spectral resolution of the instrument is ~7 nm. The instrument has a built-in wavelength calibration target plate to calibrate reflectance spectra and is capable to measure spectra from 10 s to around 5 min. Speed. The instrument is provided with PIMA View Graph™ software (version 3.1; Integrated Spectronics Pty Ltd., Baulkham Hills, Australia) to process and study the spectra of the samples. Also, the samples used for spectral measurement and thin section preparation were further powdered and analyzed using an X-ray diffractometer (MiniFlex 600, Rigaku Corporation, Japan) to confirm the minerals of the geological formations.

5 | RESULTS AND DISCUSSION

5.1 | ASTER mapping of gypsum occurrences

Figure 7a is the FCC image of ASTER (R:7; G:3; B:2) developed by selecting the bands 7, 3, and 2 which have closer wavelengths band positioning to the bands 12, 8, and 4 of Sentinel-2A. The ASTER image shows the formation of laminated gypsum found with intercalations of dolomite in dark green similar to the discrimination of
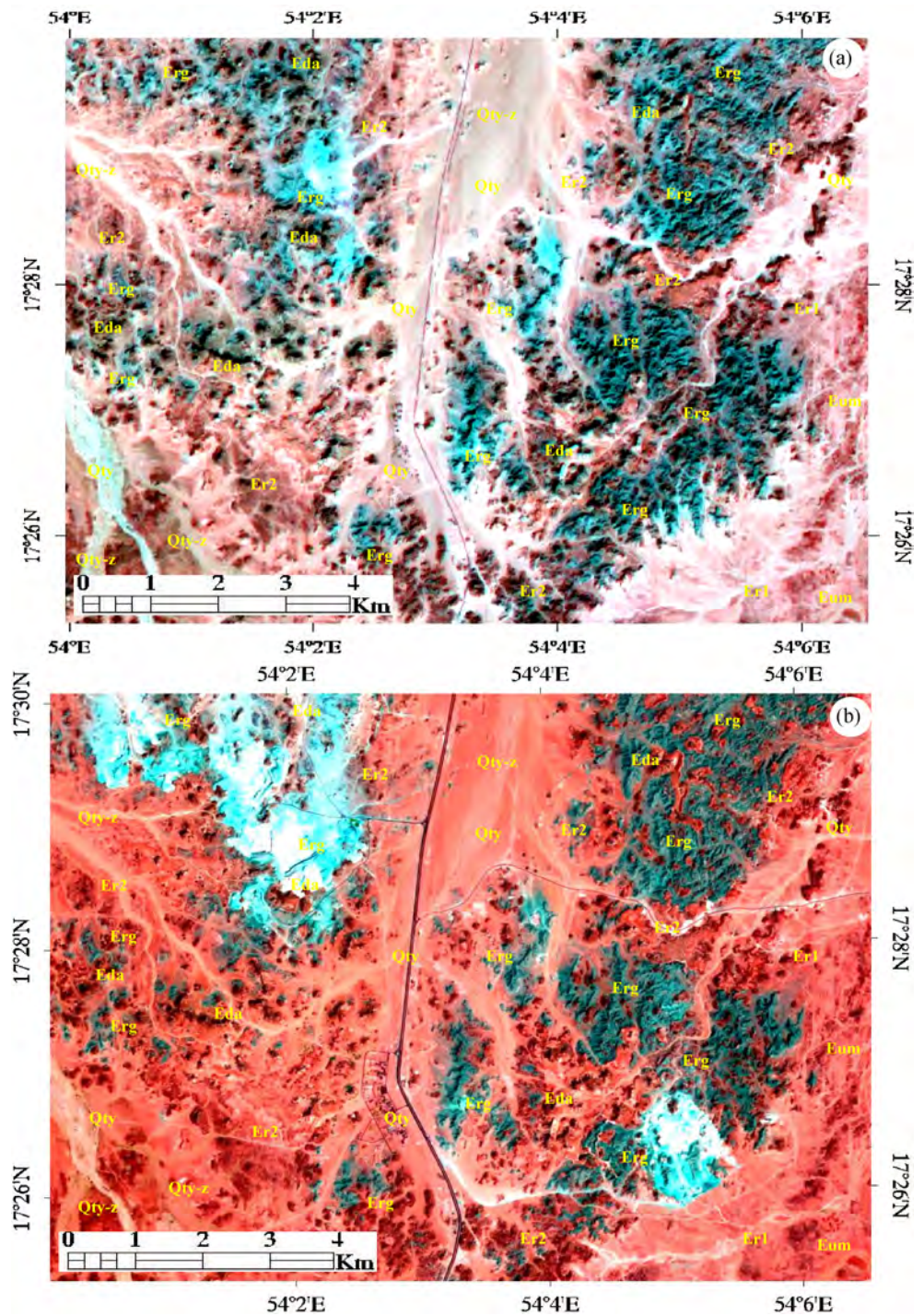
Sentinel-2A image. The formations consist of yellowish shale that occurs with intercalations bioclastic limestone, green marl, and coquina (Eda) and the recrystallized chalky dolomite found with chert, marl, and bioclastic limestone (Er2) have appeared in brown to dark brown. The wadi floor sands and gravels (Qty-z) and the Lower alluvial terrace deposits (Qty) are exhibited in very light brown to white. The image of Sentinel-2A shows the increase and change in the mining activity of the region from November 2001 to September 2018. It exhibits the geological formations little dark brown with fine texture compare to the ASTER image, which may be due to the selection of band 4 and the high spatial resolution. However, in both the images the sedimentary formations associated with the laminated gypsum are not well discriminated and showed them in shades of brown. Figure 7b shows the result of the false color composite of Sentinel-2A (R:12; G:8; B:4). Here, the band 12 (2,112.9–2,286.5 nm), which is characteristic to O—H stretching, H_2O combinations, and S—O bending overtones and stretching is selected to discriminate the formation has gypsum deposits, the band 8 (782.5 nm–887.3 nm) is chosen to highlight the other geological formation associated to the deposits, and the band 4 (649.3 nm–679.9 nm) is preferred to improve the pixel information related to recent wadi deposits by studying the images of all bands. The FCC image shows the formation of laminated gypsum and intercalations of dolomite (Erg) in dark green. The formation consists of yellowish shale with intercalations of bioclastic limestone, green marl, and coquina (Eda), and the formation occurred with the recrystallized chalky dolomite that occurred with chert, marl, and bioclastic limestone (Er2) have appeared in shades of dark brown. The wadi floor sands and gravels (Qty-z) and the Lower alluvial terrace deposits (Qty) are displayed in a bright tone.

5.2 | ASTER mapping of lithology associated with gypsum occurrences

Figure 8a is the decorrelated image (R:7; G:3; B:2) of ASTER. It shows the deposits of laminated gypsum occurred with intercalations of dolomite in blue to green. The formation consists of yellowish shale that is intercalated with bioclastic limestone, green marl, and coquina (Eda), and the formation consisting of recrystallized chalky dolomite found with chert, marl and bioclastic limestone (Er2) appears in yellowish-brown to light brown. The highly recrystallized chalky dolomite that contains the bedded chert and flint (Er1) and the thin-bedded dolomite found with chert and silica geodes (Eum) exhibits pink to red. The wadi floor sands and gravels

FIGURE 7 False color composites (FCC) of (a) ASTER (R:7; G:3; B:2). (b) Sentinel-2 (R:12; G:8; B:4) show occurrence of gypsum in dark green in the Thumrait region. Qty-z, wadi floor sand and gravel; Qty, lower alluvial terrace deposits; Eda, yellowish shale with intercalations bioclastic limestone, green marl, and coquina; Erg, laminated gypsum with intercalations of dolomite, biocalcarenite, and bedded chert and flint; Er2, partly recrystallized chalky dolomite with chert and marl and bioclastic limestone at the top; Er1, highly recrystallized chalky dolomite, bedded chert and flint; Eum, thin-bedded dolomite with chert, silica geodes

(Qty-z) and the Lower alluvial terrace deposits (Qty) appear in white to light yellow. The image shows the area of mining activity in purple-blue-green. Figure 8b shows the results of the decorrelated image (R:12; G:8; B:4) of Sentinel-2A data. The image exhibits the deposits of laminated gypsum found with intercalations of dolomite (Erg) in green. The formation consists of yellowish shale that occurred with intercalations of bioclastic limestone, green marl, and coquina (Eda) and the formation consists of

recrystallized chalky dolomite found with chert, marl, and bioclastic limestone (Er2) appear in pink-red to brown. The wadi floor sands and gravels (Qty-z) and the Lower alluvial terrace deposits (Qty) show yellow. The image of Sentinel-2A shows the area of mining in green with a smooth texture and the mining activity in purple to cyan. The decorrelated image discriminated the formations associated with layered gypsum deposits in different tones.
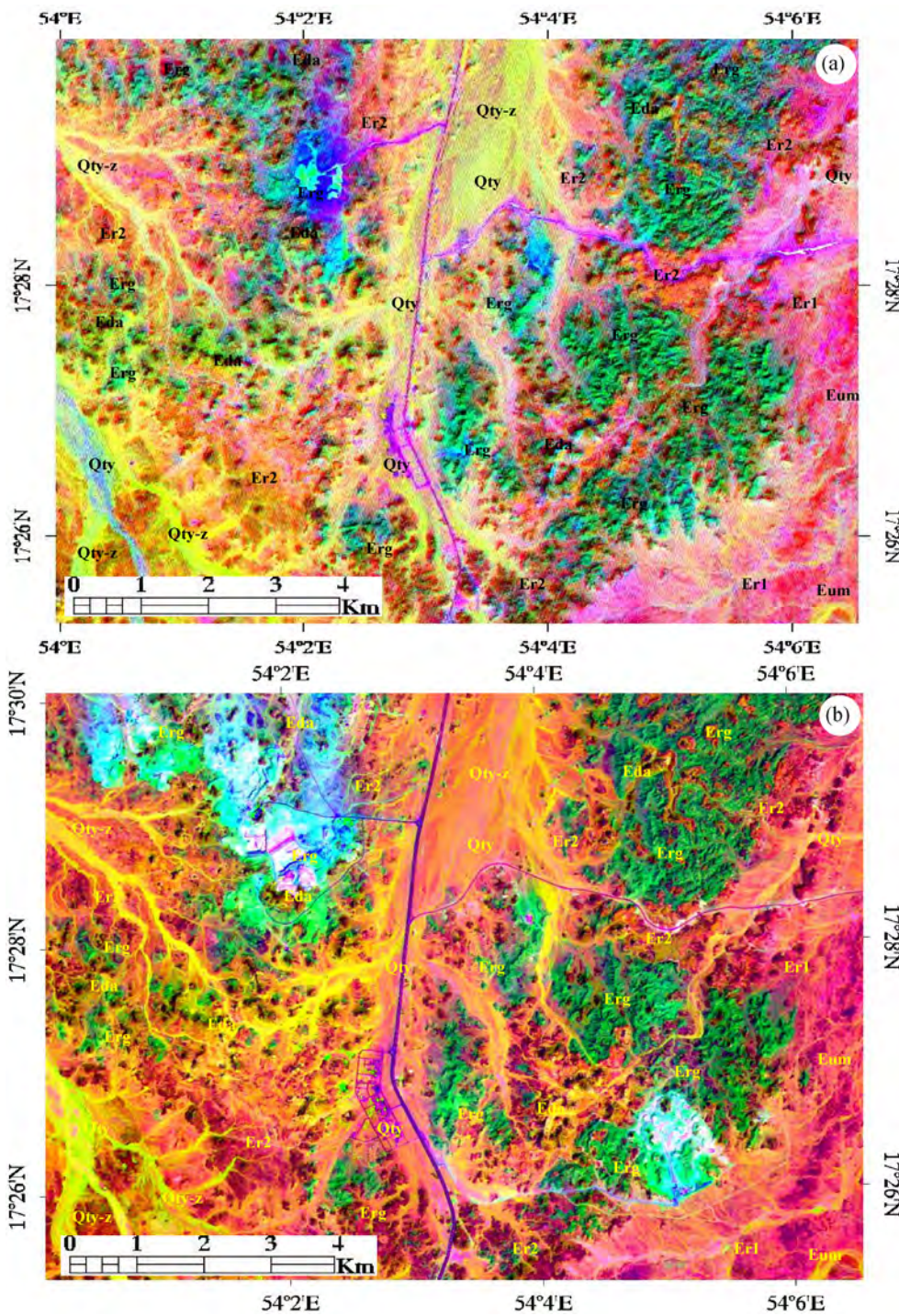
FIGURE 8 Decorrelated RGB images of (a) ASTER (R:7; G:3; B:2). (b) Sentinel-2 (R:12; G:8; B:4) show the distribution of gypsum in green in the Thumrait region. The abbreviations are as in Figure 7

5.3 | ASTER mapping of surface minerals

In this study, we mapped the surface minerals of the study area using VNIR-SWIR spectral bands of ASTER by SAM method as described in section 4.2. The classified results are studied further with the results of analyses of the VNIR-SWIR spectral bands of Sentinel-2A carried out to the area using the same procedure. The details on the

number of pixels collected, the colors selected to the spectra (minerals), and the plot of endmember spectra and area of laminated gypsum classified by the SAM are given in Figure 9. The details on the number of pixels with their relative percentages and the total area of their distribution are given in Table 2a. The end member spectral plot of the study region showed absorptions in the spectral bands 3 (760–860 nm), 5 (2145–2,185 nm), and 8 (2295–2,365 nm) (Figure 9c) which are characteristics
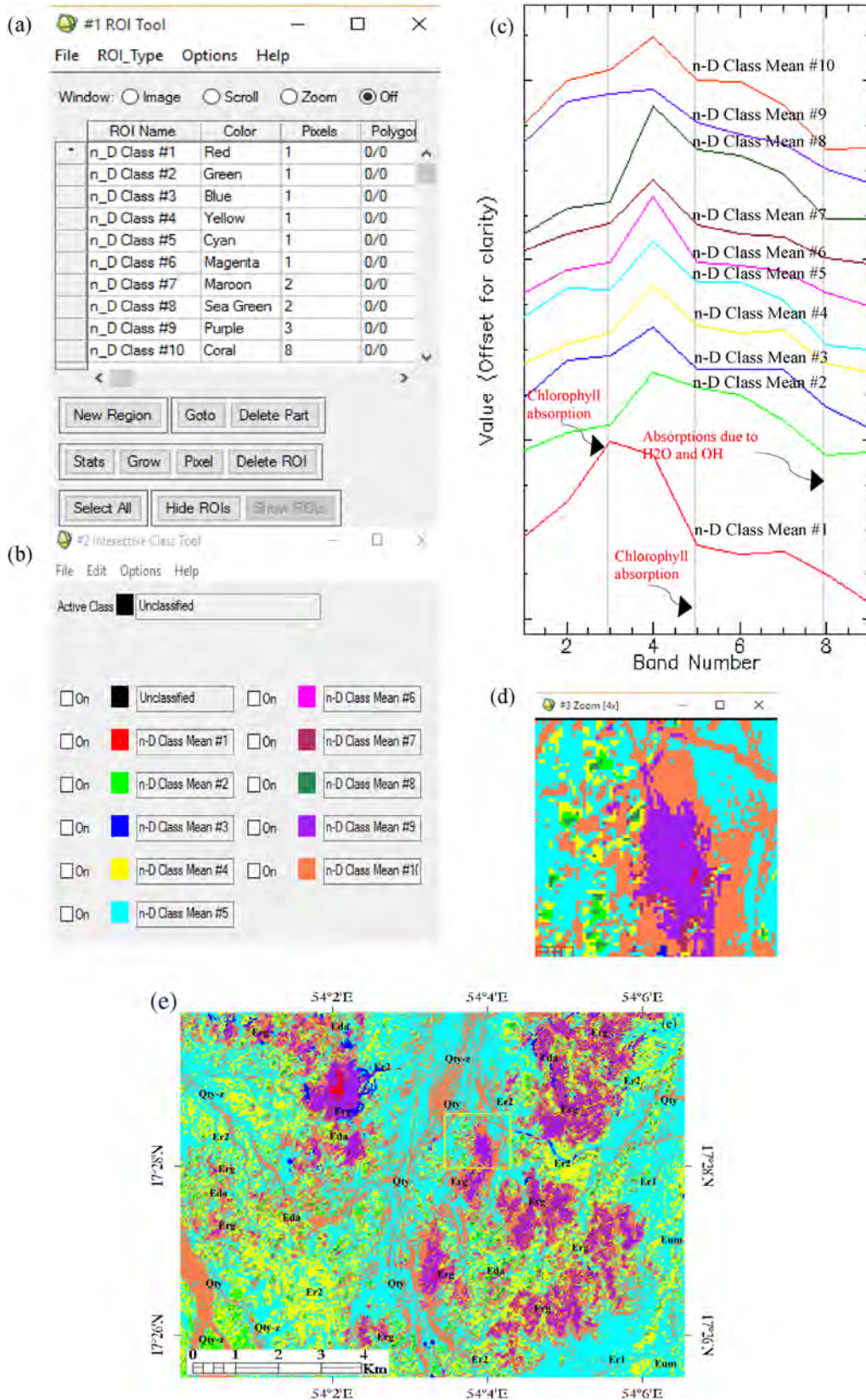
FIGURE 9 (a) The number of pixels collected on the end members. (b) The selected colors to spectra and minerals. (c) The plot of end member spectra. (d) The area of laminated gypsum. (e) The SAM image (abbreviations are as in Figure 7, the rectangle represents Figure 9d) using ASTER data

(a) n-D Classesª	No. of pixels	% in total area	Area in Km²
Unclassified	21	0.006	0.0047
n-D class mean #1	458	0.139	0.103
n-D class mean #2	6924	2.102	1.5579
n-D class mean #3	2771	0.841	0.6234
n-D class mean #4	66868	20.300	15.0454
n-D class mean #5	135258	41.064	30.4332
n-D class mean #6	121	0.037	0.0272
n-D class mean #7	14016	4.255	3.1536
n-D class mean #8	5946	1.805	1.3378
n-D class mean #9	20413	6.197	4.5929
n-D class mean #10	76598	23.254	17.2346
Total	3,29,394	100	74.1137
(b) n-D Classesª	No. of pixels	% in total area	Area in Km²
Unclassified	0	0.000	0
n-D class mean #1	40	0.004	0.0040
n-D class mean #2	6507	0.632	0.6507
n-D class mean #3	490783	47.661	49.0783
n-D class mean #4	225	0.022	0.0225
n-D class mean #5	77294	7.506	7.7294
n-D class mean #6	341983	33.211	34.1983
n-D class mean #7	8830	0.858	0.8830
n-D class mean #8	94247	9.153	9.4247
n-D class mean #9	1734	0.168	0.1734
n-D class mean #10	1207	0.117	0.1207
n-D class mean #11	6880	0.668	0.6880
Total	1,029,730	100	102.9730

TABLE 2 Distribution of pixels of Thumrait region in the (a) ASTER SAM n-D classes and (b) Sentinel-2 SAM n-D classes

of iron, Al-OH and carbonate-rich minerals of the region. The SAM image (Figure 9d,e) shows pixels classified mainly in the n-D classes #4, #5, #7, #9, and #10. The n-D classes #1, #2, #3, #6, and #8 are not classified pixels significantly (Table 2a). The n-D classes #4 and #5 predominantly classified the region by yellow and cyan pixels about 15.04 and 30.43 km² respectively. The spectra of the classes exhibited absorptions in the bands 3, 5, and 8 (Figure 9c). The absorptions may be due to the presence of iron (III) inclusions in the microcrystalline cherts and flints, and the hydroxyl and Al-OH contents in the chalky dolomites and marls which contain variable amounts of clays in the Tertiary formations of Eum, Er1, and Er2 (Figure 1). The pixels of maroon (about 3.15 km²) and purple (about 4.59 km²) are distributed within the yellow where the regions of laminated gypsums and intercalations of dolomite, biocalcarenite and bedded chert and flint (Erg) are distributed. The spectra of the n-D classes #7 and #9 showed the absorptions in

the spectral bands 3, 5, and 8. These absorptions may be due to the presence of dihydrates in the gypsum and carbonates in the dolomites minerals of the formations. The pixels are well representing the minerals found in the working and old mine sites (Figures 1, 7a, and 8a). The pixels of n-D class #10 appeared in coral (about 17.23 km²) and distributed where the Quaternary deposits (Qty-z, Qty) present (Figure 1). The spectra show absorptions in the spectral bands 3, 5, and 8. The absorptions may be due to the presence of iron (III) inclusions in the microcrystalline cherts and flints, the hydroxyl and Al-OH contents in the chalky dolomites and marls, and the carbonates contents in the dolomites, which are found as sands, and gravels in the wadi floor and terrace deposits of the study area. The red pixels of n-D class #1 distributed within the mining site and the spectra of the class show absorption in band 5, which may represent the occurrence of gypsum in the site. The absorption may be due to the presence of dihydrates in the gypsum. Also,

the green and the sea-green of the n-d classes #2 and #8 are distributed in the Tertiary formations where the chalky dolomites are present. The spectra of the classes show absorption in 3, 5, and 8, which may be due to the presence of iron (III) inclusions in the microcrystalline cherts and flints and the hydroxyl and Al-OH contents in the chalky dolomites and marls of the formations. ASTER detected the minerals of the area in the bands 3, 5, and 8, which are characteristics to the presence of iron, water, Al-OH, and CO_3 contents in the minerals of the different formations of the area.

The classified results are studied further with the results of analyses of the VNIR-SWIR spectral bands of Sentinel-2A carried out to the area using the same procedure. The details on the number of pixels collected, the colors selected to the spectra (minerals), the plot of endmember spectra, and the area of laminated gypsum classified by the SAM are given in Figure 10. The details on the number of pixels with their relative percentages and the total area of their distribution are given in Table 2b. The end member spectral plot of the region showed absorptions mainly in the spectral bands 2 (560 nm), 5 (740 nm), 7 (842 nm), and 10 (2,190 nm) (Figure 10c) which are characteristics to the presence of water, OH, and CO_3 contents in the minerals of the study area where no much vegetation is found and exposed directly to the sensor of Sentinel-2A. The SAM image (Figure 10d,e) shows pixels classified mainly in the n-D classes #3, #5, #6, and #8 (Table 2b). The other n-D classes are not classified pixels significantly. The n-D classes #3 and #5 classified the regions of 1) the laminated gypsum and intercalations of dolomite, biocalcarenite, and bedded chert and flint (Erg) and 2) the wadi floor deposits (Qty-z) (Figure 1) by blue and cyan pixels about 49 and 7.73 km^2, respectively. The spectra of the classes show absorptions in the spectral bands 7 (Figure 10c) which may characteristics of the hydroxyl contents present in the dihydrates gypsum and carbonates in the dolomites of the formation. although the spectra of n-D classes #3 are not unique to the gypsum, the band characteristic to the hydroxyl contents has classified the formations having laminated gypsum. The cyan pixels represent the area of gypsum occurrences distributed within the formation of laminated gypsums that occurred with dolomites and in the sites of gypsum mining (Figures 7b and 8b). The n-D class #6 classified pixels about 34.19 km^2 in magenta. The pixels are distributed in the area of the other sedimentary formations (Eum, Er1, and Er2) including the alluvial terrace deposits (Qty). The formations occur mainly with chalky dolomites, marls, cherts, and flints. The spectra of the class show strong absorptions in the bands 2 and 5 (Figure 10c) which may be due to the presence of iron (III) inclusions

in the microcrystalline cherts and flints, and the hydroxyl and Al-OH contents in the chalky dolomites and marls which contain variable amounts of clays. The n-D class #8 classified pixels in sea green about 9.42 km^2 are distributed as spots within magenta, which represent the formations that occurred with the marl, chert, flint, and chalky dolomite. The spectra of the class show strong absorptions in bands 2 and 7 (Figure 10c) which may be due to the presence of the hydroxyl contents in the marl and chalky dolomite. The pixels of the n-D classes #2, #7 and #11 are distributed within the sites of the mining of gypsum where the green pixels (n-D class #2) represent the dumped area of dolomite (separated from gypsum while mining), the maroon pixels (n-D class #7) show the area of seized gypsum dumped for export and the pixels of aquamarine (n-D class #11) represent the mining sites. These were verified during fieldwork supported by the high-resolution Google Earth images. All the spectra of the study area show absorptions in the spectral bands 2, 5, and 7 which are due to the presence of iron (III) inclusions in the microcrystalline chert and flints the hydroxyl, and Al-OH contents in the chalky dolomite and marl, the dihydrates in the gypsum, and the carbonates in the dolomite. In the plot, all spectra show absorptions toward the band 10, which may represent that the study area has the distribution of marls and chalky dolomite rich soil. Overall, the spectral bands 2, 5, 7, and 10 characteristics to the absorptions of the green peak, red edge, LAI (leaf area index), and clay soil erosion (Drusch et al., 2012; van der Meer et al., 2014) are detected the minerals which are characteristics to the iron, water, OH, and CO_3 contents in the region. The minerals detected by the Sentinel (Figure 10e) are comparable with the results of the ASTER (Figure 9e) and the data of Sentinel-2A can be used in the arid region.

6 | FIELD AND LABORATORY STUDIES

Field study is conducted in and around the Thumrait region to validate the image results and mapping of the gypsum and the associated formations. In the field, the Tertiary formations occur as small hills with abundant laminated gypsum and intercalations of dolomite, biocalcarenite, and bedded chert, flint (Erg; Figure 11a), and laminated partly recrystallized white chalky dolomite, collapse breccia, chert beds, with marl and bioclastic limestone (Er2; Figure 11b). The occurrences are verified with the image results and confirmed. The laminated gypsum occurs at the top of older chalky dolomite (Figure 11c) and fragments of calcarenites and bedded cherts (Figure 11b,c) which covers the boundary between
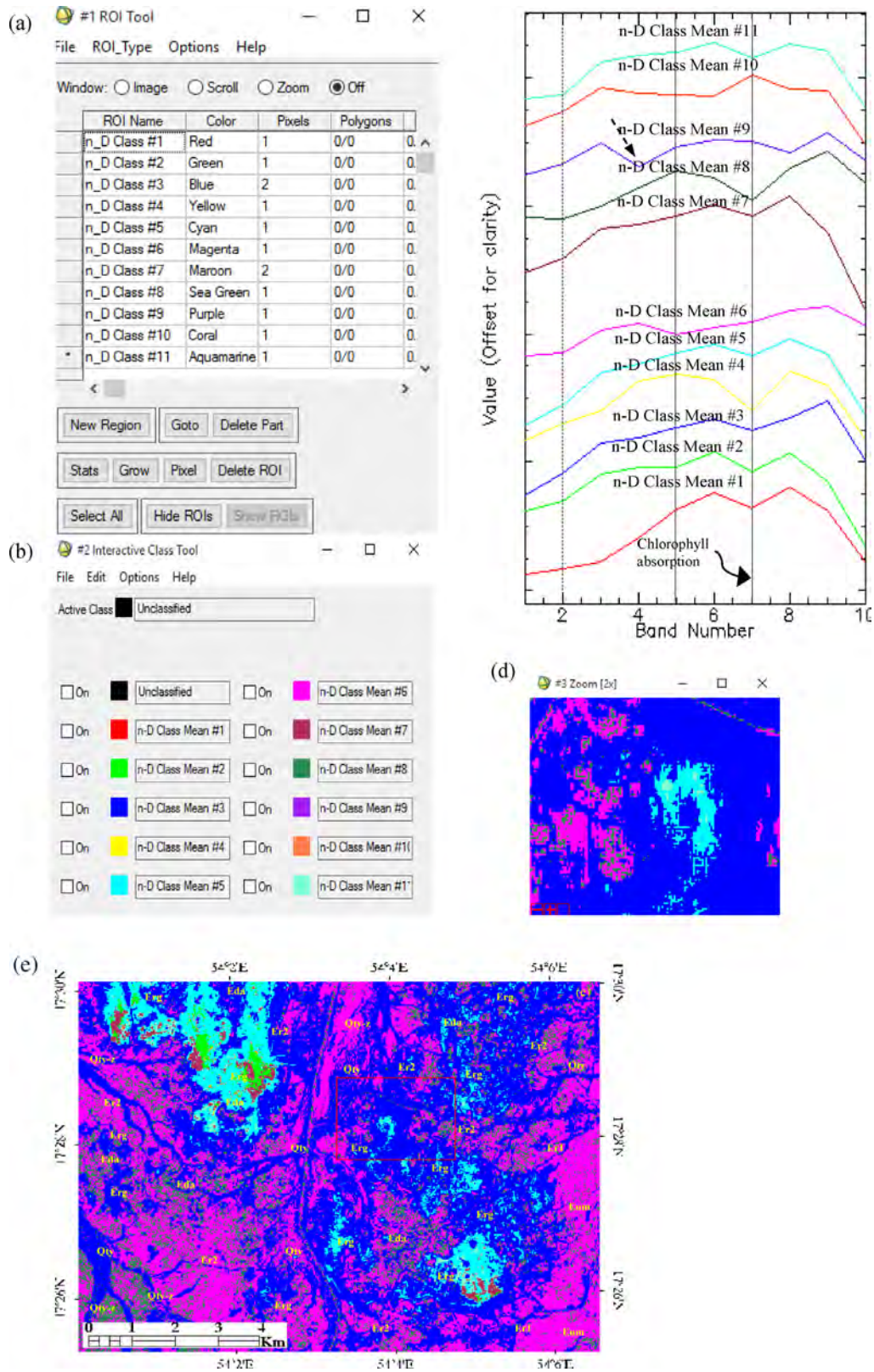
FIGURE 10 (a) The number of pixels collected on the end members. (b) The selected colors to spectra and minerals. (c) The plot of end member spectra. (d) The area of laminated gypsum. (e) The SAM image (abbreviations are as in Figure 7, the rectangle represents Figure 8d) using Sentinel-2A data

FIGURE 11 Field photographs showing the occurrence of (a-c) the laminated gypsums and chalky dolomites. (d) The calcarenites and cherts. (e) The laminated gypsum with shale. (f) The yellowish shale and bioclastic limestones. (g) The crystallized gypsum. (h) The quaternary wadi deposits
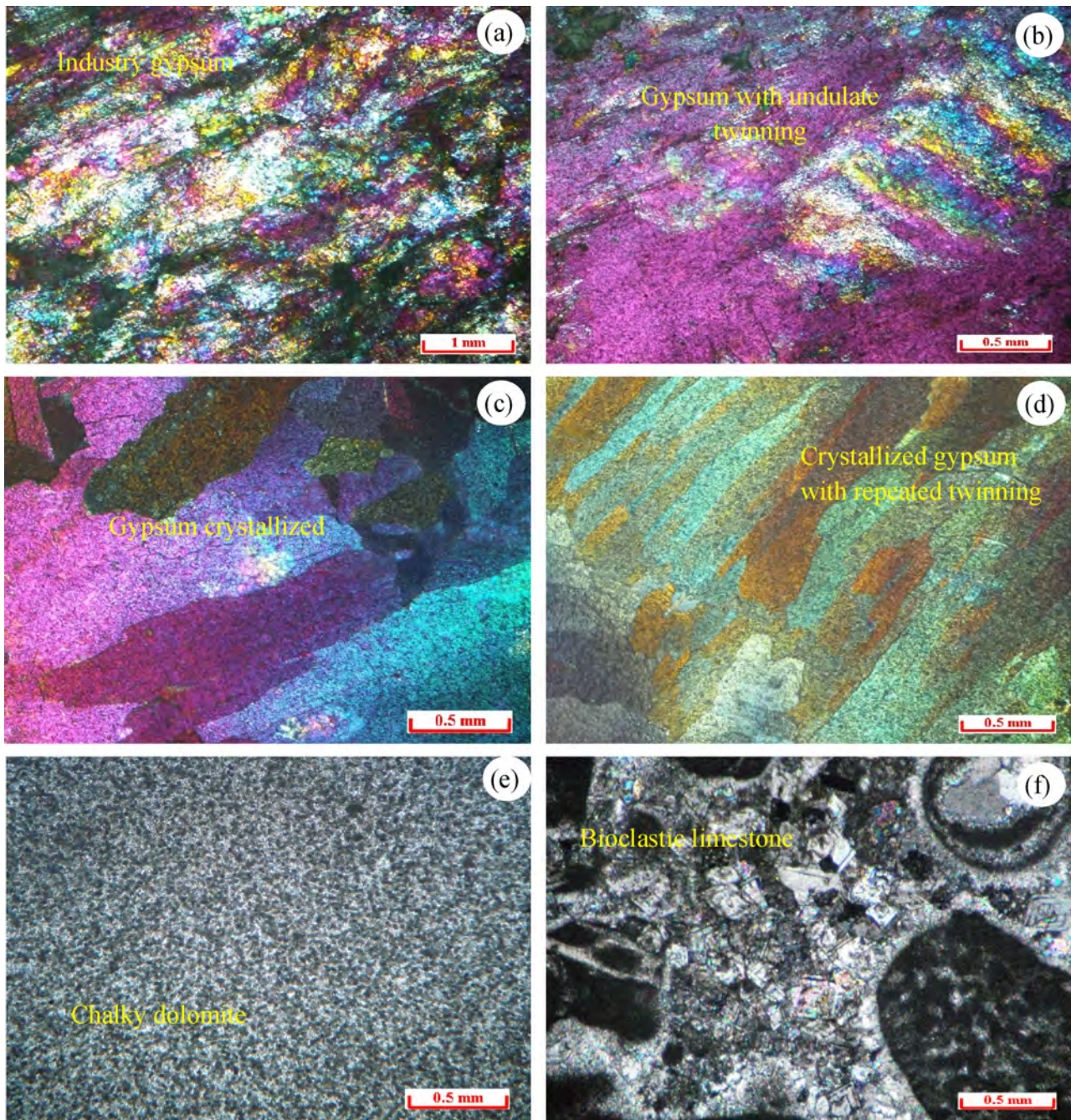
FIGURE 12 Microphotographs showing (a) the fined grained. (b) Undulated twinning in the industrial gypsum. (c) The coarse-grained. (d, e) Repeated twinning with perfect cleavage in the crystallized gypsum. (f) The dolomite in the chalky dolomite. (g) Calcite with fossils in bioclastic limestone under the parallel and crossed nicols

the formations (Figure 11d). Occurrences of laminated gypsum are well exposed in the road cuttings and mine sites (Figure 11e). The occurrence of yellowish shale with intercalations of white to yellowish bioclastic limestone, green marl, and coquina (Eda) are found at the top of the laminated gypsum formations (Figure 11f). Presence of the dumped area of dolomites (separated from mining), the area of seized gypsum dumped for export, and the

mining sites are verified in the area of mining. There are numerous thin layers found with well-crystallized gypsums in between the yellowish shale and bioclastic limestone formations (Figure 11g). The quaternary deposits (Figure 11h) are the sands and gravels that occurred on the wadi floor and alluvial terrace.

To validate the spectral characters of gypsum, chalky dolomite, bioclastic limestone, and yellowish shale, the

FIGURE 13 Results of XRD analyses of (a) the industrial gypsum (no IG3). (b) The gypsum of sedimentary formations (no SG2). (c) The chalky dolomites (no Dl7). (d) The calcites in the yellowish bioclastic limestones (no Bl9)

interpretations of ASTER and Sentinel-2A images and the field characters of Tertiary formations, the samples collected from the field are studied for mineralogical characters using a microscope and by XRD method. Under the microscope, the industry gypsums are fine-grained exhibited undulated twining and first-order interference colors (Figure 12a,b). The crystallized gypsums exhibit perfect cleavage, multiple twining, and typical first-order interference colors (Figure 12c,d). The samples of chalky dolomite showed the presence of very fine-grained dolomite minerals (Figure 12e) and the bioclastic limestones showed the presence of calcites with fossils (Figure 12f). The thin sections of the shale formations showed the presence of illite and kaolinite. The analysis of the field samples by the XRD method confirmed further the presence of gypsum minerals in the laminated gypsum and crystallized gypsum (Figure 13a,b; Samples no IG3 and SG2), the dolomite in the chalky dolomite (Figure 13c; Sample no Dl7) and the calcites with fossils in the yellowish bioclastic limestone (Figure 13d; Sample no Bl9) formations of the study area.

7 | CONCLUSIONS

In this study, we processed the spectral bands of ASTER and mapped the laminated gypsum occurrences and associated geological formations of the area near Thumrait region southern Oman. The spectra measured for gypsum samples showed the spectral absorptions in between 1,400–1,600, 1,750 1,940, 2,200, and 2,400 nm; the chalky dolomite exhibited the absorptions near 1,400, 1,900, 2,160, 2,335, and 2,490 nm; the bioclastic limestone showed absorptions similar to chalky dolomite except showing deep absorptions and difference in values near 2,345 and 2,495 nm; and the shale showed absorptions near 1,400, 1,900, and 2,350 nm comparable with the USGS spectral library for minerals. The spectral plot of the industrial gypsum and the gypsum of sedimentary formations of the study area resampled to SWIR spectral bands (4 to 9) of ASTER in 1.3 to 2.5 μm showed clearly the absorptions in the 2.2 and 2.4 μm. The study of spectral bands 7, 3, and 2 of ASTER and the false color composite developed using the bands discriminated the area of gypsum occurrences. The bands processed by the decorrelation method well distinguished the gypsum occurrences from the other geological formations. The mapping of the surface minerals of the area using the SAM method showed the spectra of the study area have absorptions in the bands 3, 5, and 8 which may be due to the presence of iron (III) inclusions in the microcrystalline chert and flint and the hydroxyl and Al-OH contents in the chalky dolomite and marl of the formations. All

the results of ASTER are compared with the results obtained using the Sentinel-2A data, which showed that the Sentinel-2A performed similar to ASTER and can be used to map the gypsum occurrences and geological formations of the arid region. The field and laboratory studies supported the sensor's capability.

ORCID
Sankaran Rajendran https://orcid.org/0000-0002-9371-9908

REFERENCES
Abrams, M.J., Rothery, D.A. and Pontual, A. (1988) Mapping in the Oman ophiolite using enhanced Landsat thematic mapper images. *Tectonophysics*, 151, 387–401.

Abrams, M. (2000) The advanced spaceborne thermal emission and reflection radiometer (ASTER): data products for the high spatial resolution imager on NASA's Terra platform. *International Journal of Remote Sensing*, 21, 847–859.

Al-Nahmi, F., Saddiqi, O., Hilali, A., Rhinane, H., Baidder, L., El Arabi, H. and Khanbari, K. (2017) Application of remote sensing in geological mapping, case study Al Maghrabah area – Hajjah region, Yemen. *ISPRS Annals of the Photogrammetry, Remote Sensing, and Spatial Information Sciences*, IV-4/W4, 63–71.

Atzberger, C. and Richter, K. (2012) Spatially constrained inversion of radiative transfer models for improved LAI mapping from future Sentinel-2 imagery. *Remote Sensing of Environment*, 120, 208–218.

Bishop, J.L. and Murad, E. (2005) The visible and infrared spectral properties of jarosite and alunite. *American Mineralogist*, 90, 1100–1107.

Blaney, D.L. and McCord, T.B. (1995) Indications of sulfate minerals in the Martian soil from earth-based spectroscopy. *Journal of Geophysical Research*, 100, 14433–14441.

Boardman, J.W. and Kruse, F.A. (1994) Automated spectral analysis: a geological example using AVIRIS data, north grapevine mountains, Nevada. Paper presented at proceedings, ERIM tenth thematic conference on geologic remote sensing. Environmental Research Institute of Michigan, Ann Arbor, MI I-407-I-418.

Cardoso-Fernandes, J., Cardoso-Fernandes, J., Lima, A., Lima, A., Teodoro, A.C. and Teodoro, A.C. (2018) Potential of Sentinel-2 data in the detection of lithium (Li)-bearing pegmatites: a study

case. *Proc. SPIE*, 10790, 107900T. https://doi.org/10.1117/12.2326285.

Clark, R.N., King, T.V.V., Klejwa, M., Swayze, G. and Vergo, N. (1990) High spectral resolution reflectance spectroscopy of minerals. *Journal of Geophysical Research.*, 95, 12653–12680.

Clark, R.N., Swayze, G.A., Gallagher, A.J., King, T.V.V., and Calvin, W.M. (1993) Digital spectral library: version 1: 0.2 to 3.0 microns. *U.S.Geological Survey Open File Report*, 93–592.

Clark, R.N., Swayze, G.A., Wise, R., Livo, E., Hoefen, T., Kokaly, R. and Sutley, S.J. (2007) USGS digital spectral library splib06a: U.S. Geological Survey, Digital Data Series 231.

Clevers, J.G.P.W. and Gitelson, A.A. (2013) Remote estimation of crop and grass chlorophyll and nitrogen content using red-edge bands on Sentinel-2 and -3. *International Journal of Applied Earth Observation and Geoinformation*, 23, 344–351.

Cloutis, E.A., Hawthorne, F.C., Mertzman, S.A., Krenn, K., Craig, M.A., Marcino, D., Methot, M., Strong, J., Mustard, J.F., Blaney, D.L., Bell, J.F. and Vilas, F. (2006) Detection and discrimination of sulfate minerals using reflectance spectroscopy. *Icarus*, 184, 121–157.

Cloutis, E.A., Craig, M.A., Kruzelecky, R.V., Jamroz, W.R., Scott, A., Hawthorne, F.C. and Mertzman, S.A. (2008) Spectral reflectance properties of minerals exposed to simulated Mars surface conditions. *Icarus*, 195, 140–168.

Costa, S., Santos, V., Melo, D. and Santos, P. (2017). Evaluation of Landsat 8 and sentinel-2A data on the correlation between geological mapping and NDVI. Paper presented at: First IEEE International Symposium of Geoscience and Remote Sensing (GRSS-CHILE).

Crowley, J.K. (1991) Visible and near-infrared (0.4–2.5 µm) reflectance spectra of playa evaporite minerals. *Journal of Geophysical Research: Solid Earth*, 96, 16231–16240.

Delegido, J., Verrelst, J., Meza, C.M., Rivera, J.P., Alonso, L. and Moreno, J. (2013) A red-edge spectral index for remote sensing estimation of green LAI over agroecosystems. *European Journal of Agronomy*, 46, 42–52.

Drusch, M., Del Bello, U., Carlier, S., Colin, O., Fernandez, V., Gascon, F., Hoersch, B., Isola, C., Laberinti, P. and Martimort, P. (2012) Sentinel-2: ESA's optical high-resolution mission for GMES operational services. *Remote Sensing of Environment*, 120, 25–36.

D'Odorico, P., Gonsamo, A., Damm, A. and Schaepman, M.E. (2013) Experimental evaluation of Sentinel-2 spectral response functions for NDVI time-series continuity. *IEEE Transactions on Geoscience and Remote Sensing*, 51, 1336–1348.

Frampton, W.J., Dash, J., Watmough, G. and Milton, E.J. (2013) Evaluating the capabilities of Sentinel-2 for quantitative estimation of biophysical variables in vegetation. *ISPRS Journal of Photogrammetry and Remote Sensing*, 82, 83–92.

Gabr, S., Ghulam, A. and Kusky, T. (2010) Detecting areas of high-potential gold mineralization using ASTER data. *Ore Geology Reviews*, 38, 59–69.

Gastellu-Etchegorry, J.P., van der Meer Mohr, H., Handaya, A. and Surjanto, W.J. (1990) An evaluation of SPOT capability for mapping the geology and soils of Central Java. *International Journal of Remote sensing*, 11(4), 685–701.

Ge, W., Cheng, Q., Jing, L., Armenakis, C. and Ding, H. (2018a) Lithological discrimination using ASTER and Sentinel-2A in the Shibanjing ophiolite complex of Beishan orogenic in Inner Mongolia, China. *Advances in Space Research*, 62(7), 1702–1716.

Ge, W., Cheng, Q., Tang, Y., Jing, L. and Gao, C. (2018b) Lithological classification using sentinel-2A data in the Shibanjing Ophiolite complex in Inner Mongolia, China. *Remote Sensing*, 2018(10), 638. https://doi.org/10.3390/rs10040638.

Gillespie, A.R., Kahle, A.B. and Walker, R.E. (1996) Color enhancement of highly correlated images. I. Decorrelation and HSI contrast stretches. *Remote Sensing of Environment*, 20, 209–735.

Hedley, J., Roelfsema, C., Koetz, B. and Phinn, S. (2012) Capability of the sentinel 2 mission for tropical coral reef mapping and coral bleaching detection. *Remote Sensing of Environment*, 120, 145–155.

Hunt, G.R. (1977) Spectral signatures of particulate minerals in the visible and near infra-red. *Geophysics*, 42, 501–513.

Hunt, G.R., Salisbury, J.W. and Lenhoff, C.J. (1971) Visible and near-infrared spectra of minerals and rocks. VI. Sulfides and sulfates. *Modern Geology*, 3, 1–14.

Hunt, G.R. and Salisbury, J.W. (1971) Visible and near infrared spectra of minerals and rocks: II. Carbonates. *Modern Geology*, 2, 23–30.

Hosseinjani Zadeh, M., Tangestani, M.H., Roldan, F.V. and Yusta, I. (2014) Spectral characteristics of minerals in alteration zones associated with porphyry copper deposits in the middle part of Kerman copper belt, SE Iran. *Ore Geology Reviews*, 62, 191–198.

Kruse, F.A., Lefkoff, A.B., Boardman, J.B., Heidebreicht, K.B., Shapiro, A.T. and Barloon, P.J. (1993) The spectral image processing system (SIPS)—interactive visualization and analysis of imaging spectrometer data. *Remote Sensing of Environment*, 44, 145–163.

Matthews, J.P. and Jones, A.S.G. (1992) Mapping the Xigaze (Tibet) ophiolite complex with Landsat thematic mapper data. *Journal of Himalayan Geology*, 3, 97–101.

Mars, J.C. and Rowan, L.C. (2010) Spectral assessment of new ASTER SWIR surface reflectance data products for spectroscopic mapping of rocks and minerals. *Remote Sensing of Environment*, 114, 2011–2025.

Mielke, C., Bösche, N.K., Rogass, C., Segl, K., Gauert, C. and Kaufmann, H. (2014) Potential applications of the Sentinel-2 multispectral sensor and the ENMAP hyperspectral sensor in mineral exploration. *EARSeL eProceedings*, 13, 93–102.

Ministry of Petroleum and Minerals. (1988) Geological map of Salalah, Sultanate of Oman (scale 1:100,000). Sheet NE 40-9D.

Padró, J.C., Muñoz, F.J., Ávila, L.A., Pesquer, L. and Pons, X. (2018) Radiometric correction of Landsat-8 and sentinel-2A scenes using drone imagery in synergy with field Spectroradiometry. *Remote Sensing*, 10, 1687. https://doi.org/10.3390/rs10111687.

Pour, A.B. and Hashim, M. (2012) The application of ASTER remote sensing data to porphyry copper and epithermal gold deposits. *Ore Geology Reviews*, 44, 1–9.

Rajendran, S., Nasir, S. and Al Jabri, K. (2020) Mapping and accuracy assessment of siltation of recharge dams using remote sensing technique. *Scientific Reports*, 10, 10364.

Rajendran, S. and Nasir, S. (2019) ASTER capability in mapping of mineral resources of arid region: a review on mapping of mineral resources of the Sultanate of Oman. *Ore Geology Reviews*, 108, 33–53.

Rajendran, S., Nasir, S., El-Ghali, M., Alzebdah, K., Al-Rajhi, A.S. and Al-Battashi, M. (2018) Spectral signature characterization and remote mapping of Oman exotic limestones for industrial rock resource assessment. *Geosciences*, 8(145), 1–18.

Richter, K., Atzberger, C., Vuolo, F., Weihs, P. and D'Urso, G. (2009) Experimental assessment of the Sentinel-2 band setting for RTM-based LAI retrieval of sugar beet and maize. *Canadian Journal of Remote Sensing*, 35, 230–247.

Richter, K., Hank, T.B., Vuolo, F., Mauser,W. and D'Urso, G. (2012) Optimal exploitation of the Sentinel-2 spectral capabilities for crop leaf area index mapping. *Remote Sensing*, 4, 561–582.

Rothery, D.A. (1987) Decorrelation stretching an aid to image interpretation. *International Journal of Remote Sensing*, 8, 1253–1254.

Rowan, L.C. and Mars, J.C. (2003) Lithologic mapping in the mountain pass, California area using advanced Spaceborne thermal emission and reflection radiometer (ASTER) data. *Remote Sensing of Environment*, 84, 350–366.

Salama, M.S., Radwan, M. and van der Velde, R. (2014) A hydro-optical model for deriving water quality variables from satellite images (HydroSat): a case study of the Nile River demonstrating the future Sentinel-2 capabilities. *Physics and Chemistry of the Earth, Parts A/B/C*, 50–52, 224–232.

Tangestani, M.H., Jaffari, L., Vincent, R.K. and Maruthi Sridhar, B. B. (2011) Spectral characterization and ASTER-based lithological mapping of an ophiolite complex: a case study from Neyriz ophiolite, SW Iran. *Remote Sensing of Environment*, 115, 2243–2254.

van der Meer, F.D., van der Werff, H.M.A. and van Ruitenbeek, F.J. A. (2014) Potential of ESA's Sentinel-2 for geological applications. *Remote Sensing of Environment*, 148, 124–133.

van der Werff, H. and van der Meer, F. (2015) Sentinel-2 for mapping iron absorption feature parameters. *Remote Sensing*, 7, 12,635–12,653.

Verrelst, J., Munoz, J., Alonso, L., Delegido, J., Rivera, J.P., Camps-Valls, G. and Moreno, J. (2012) Machine learning regression algorithms for biophysical parameter retrieval: opportunities for Sentinel-2 and -3. *Remote Sensing of Environment*, 118, 127–139.

Yamaguchi, Y., Kahle, A.B., Tsu, H., Kawakami, T. and Pniel, M. (1998) Overview of advanced Spaceborne thermal emission and reflection radiometer (ASTER). *IEEE Transactions on Geoscience and Remote Sensing*, 36, 1062–1071.

Yuhas, R.H., Goetz, A.F.H. and Boardman, J.W. (1992) Discrimination among semi-arid landscape endmembers using the spectral angle mapper (SAM) algorithm. *JPL Publications*, 4(92–41), 147–149.